Harvesting a wide spectral range of electronic coherences with disordered quasi-homo dimeric assemblies at room temperature

James Hamilton,[1] Edoardo Amarotti,[2†] Carlo Nazareno Dibenedetto,[3,4]
Marinella Striccoli,[3] R. D. Levine,[5] Elisabetta Collini,[2] F. Remacle[1*]

[1]*Department of Theoretical Physical Chemistry, University of Liège, B4000 Liège, Belgium*

[2] *Department of Chemical Sciences, University of Padova, Padova, Italy.*

[3]*CNR-IPCF SS Bari, c/o Chemistry Department, University of Bari Aldo Moro, Bari, Italy*

[4] *Chemistry Department, University of Bari Aldo Moro, Bari, Italy*

[5]*The Fritz Haber Research Center for Molecular Dynamics and Institute of Chemistry, The Hebrew University of Jerusalem, Jerusalem 91904, Israel*

James Hamilton: james.hamilton@uliege.be

Edoardo Amarotti: edoardo.amarotti@chemphys.lu.se
† Present address: Division of Chemical Physics and NanoLund, Lund University, P.O. Box 124, 22100 Lund, Sweden

Carlo Nazareno Dibenedetto: c.dibenedetto@ba.ipcf.cnr.it

Marinella Striccoli: m.striccoli@ba.ipcf.cnr.it

Raphael D. Levine: raphy@mail.huji.ac.il

Elisabetta Collini: elisabetta.collini@unipd.it

* Francoise Remacle: fremacle@uliege.be, corresponding author

Keywords: multi-layered assemblies of CdSe quantum dots, coherent coupling in quantum dot quasi-dimers, size dispersion, quantum dots for quantum information processing, 2 and multi-dimensional electronic spectroscopy

Abstract

A wide variety of photoinduced electronic coherences are shown to be robust with respect to dephasing in ensembles of quasi-homodimers assembled with sub-nm ligands from colloidal 3 nm CdSe quantum dots (QDs) with controlled 9% size dispersion, both in solution and in solid-state. Coherence periods ranging from 40 to 300 fs are consistently characterized by multi-dimensional electronic spectroscopy in the Vis range in solution and solid-state samples. A theoretical model that includes size dispersion, spin orbit coupling, and crystal field splitting supports the assignment of electronic coherences. Further, this model provides a guide for optimizing the coherences by tuning the interplay between dimer electronic delocalization, optical activity and size dispersion. The experimental persistence of many QD electronic coherences at the level of the size dispersed ensemble in the solid-state and in solution opens the way for building versatile bottom-up materials well suited to quantum technology applications.

TOC

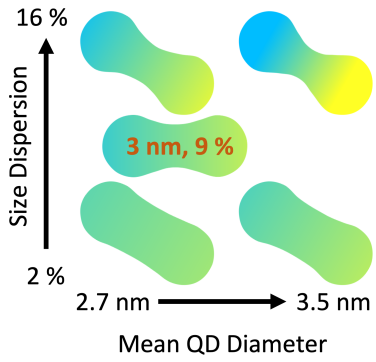

Interdot delocalization of the electronic wave function, as a function of mean diameter $\overline{D}$ and size dispersion, in a quasi-homodimers of colloidal CdSe QDs. Ensembles of $\overline{D}$ = 3nm /9% size dispersion QD's exhibit a wide range of electronic coherences observable by multi-dimensional electronic spectroscopy in solution and the solid state, providing versatile building blocks for quantum technologies

1. Introduction

Monodispersed semi-conducting nanometric QD materials have been extensively studied since the 1990s for their size-dependent, tunable electronic and optical properties.[1-8] They have recently received renewed attention as versatile materials for quantum technologies and quantum information processing.[9-17] Coherent exciton and phonon dynamics were characterized in isolated QDs by 2-dimensional electronic spectroscopy (2DES)[18-24] and transient absorption[25-26] which opens the way for applications exploiting coherent superpositions of quantum states as targeted in the second quantum revolution.

Colloidal QDs can be organized in larger structures. The ability to achieve narrow size dispersion in colloidal synthesis enables the engineering of self-assembly in superlattices.[27-30] Recently, efficient electronic delocalization has been realized in fused colloidal core-shell CdSe/CdS QD dimers with a large size (> 6 nm diameter).[31]

Electronically coupled dimers can also be assembled from small (< 3.5 nm in diameter) CdSe colloidal QD's with narrow size distributions and short ligands to favor interdot coupling.[32-33] However, achieving high levels of monodispersity remains a challenge for such small colloidal CdSe QDs. For such small diameters, intrinsic size dispersions of between 5 and 10% remain unavoidable. At the level of the ensemble, this inherent size dispersion is the source of a dispersion in the electronic properties of the isolated QDs, which in turn leads to inhomogeneous broadening.[20, 23, 25, 34-35] This inhomogeneous broadening dominates other sources of dephasing in ensembles of small diameter (< 3.5 nm) QDs.[15, 36-37]

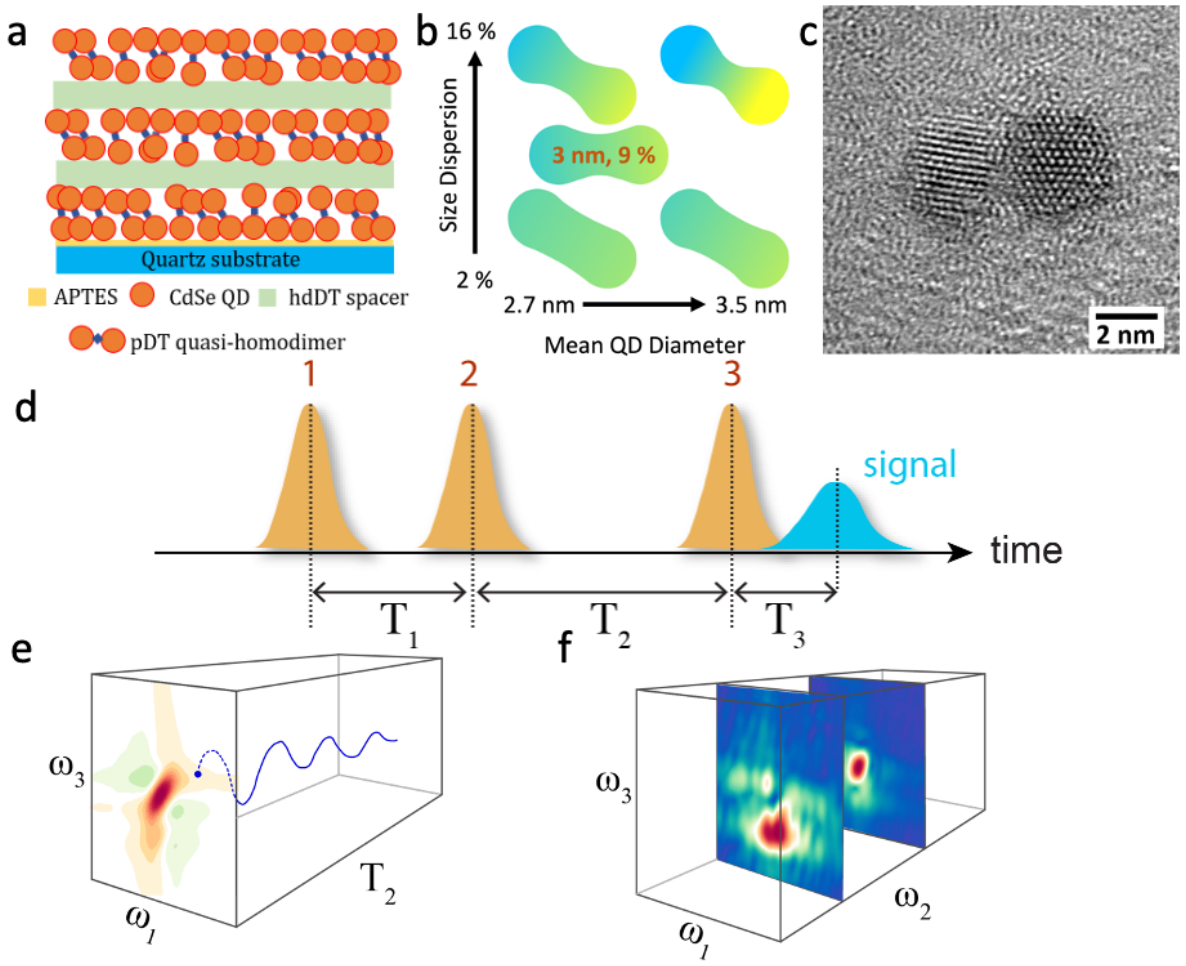

Figure 1 a) Schematics of the solid-state sample of CdSe QD quasi-homodimers (see SI for details on the assembly procedure) b) Influence of the mean QD diameter and of the size dispersion on the electronic interdot coupling. Quasi-dimers shaded in blue and yellow are not effectively electronically coupled while quasi-dimers shaded in green are effectively coupled. c) A TEM image of a quasi-homodimer assembled from 3nm QD's as used in the solid-state and solution samples. d) Sequence of three fs laser pulses as used in 2DES. e) 2D frequency maps obtained by 2DES. The time intervals T_1 and T_3 are Fourier transformed to ω_1 and ω_3 respectively and plotted as a function of T_2 which allows probing the periods of the electronic coherences between excited states. f) 3D Fourier maps. The time-interval T_2 is also Fourier transformed to ω_2, which provides a frequency mapping of the periods of the electronic coherences along T_2, see SI section S2 for details on the experimental set-up.

We report on 2DES measurements on quasi-homodimers of CdSe QDs, with a mean diameter ($\overline{D}$) of 3 nm and a size dispersion of 9%, assembled by short propanedithiol ligands as described in ref. [32], both in liquid and in solid phase, Figure 1a, b, c and Figure S1 for the histogram of the size distribution. As in our previous studies, [36-37] the sub-nanometric, ≈ 0.5 nm, surface to surface distance combined with the strong confinement effects of the QDs' small sizes, ensures an effective delocalization of the wave functions over the two QDs in the dimers of the

ensemble. While, in our previous work, the QD dimers were obtained from the deposition of the QD monomers in multilayer films,[36] in the assembly procedure used here, the dimers are first prepared in solution by partially functionalizing the QD with propanedithiol. The dimers are then deposited layer by layer in thin films, as shown in Figure 1a, using a long alkyl chain molecule, as 1,16-hexadecanedithiol as spacer between the layers. Thereby, the dimers maintain a high degree of individuality in the solid-state samples that can be directly compared to the solution ones, see section S1 of the SI for more details. The size dispersion, ≈ 9%, of the QD's used to assemble the dimers studied here is almost twice that of the ensembles studied in our previous work.[36-37] Nevertheless, our 2DES measurements on solution and solid-state samples show that the electronic coherences remain robust and can be consistently characterized at the level of the ensemble at room temperature. The novel point is that, because of the larger inhomogeneous broadening due to the larger size dispersion, it is not possible to separately resolve individual coherences in traces along T_2 at specific addresses on the 2D frequency maps, see Figure 1e. Instead, because of the inhomogeneous broadening due to size dispersion, several coherences between excited states contribute at roughly the same position on the frequency maps, as shown schematically in Figure 2b. We unambiguously characterize this richer and more complex dynamical behavior of QD dimer electronic coherences in the liquid and condensed phase using advanced tools of 2DES data analysis supported by theory and modeling. We show that the size dispersion and the mean diameter, $\overline{D}$, of the QD's in the dimers govern the spectrum of electronic coherences that can be reliably observed and subsequently exploited in bottom-up quantum devices at room temperature.

2. Theoretical modeling of ensembles of quasi-homodimers of size dispersed CdSe QDs

At the level of the ensemble, the size dispersion leads to a band structure of the exciton energies of the isolated QDs, and controls the widths of the distribution of transition frequencies.[15, 38] In strongly electronically coupled QD dimers assembled with short sub-nm ligands, resonances or quasi-resonances between the excitons of the two constitutive QDs favor the electronic coupling and the delocalization of the electronic states over the two dots.[15, 36-38] In the case of heterodimers, resonances between two excitonic bands can be tuned by adjusting the $\overline{D}$ of the two QDs[15, 33, 38-39] so as to ensure an effective electronic coupling. For dimers assembled with QDs of the same $\overline{D}$, the excitonic bands of each QD are degenerate, which leads intrinsically to a larger number of delocalized dimer states.[36-37] These are quasi-homodimers because,

although the $\overline{D}$ of the QDs constituting each dimer in the ensemble is the same, their actual size is slightly different. In such quasi-homodimers, the electronic delocalization remains strong because it takes place between electronic wave functions of states of the same nodal pattern on each dot, leading to an intrinsically stronger electronic coupling than in heterodimers. In either case, the strong confinement effects occurring in small diameter ($\overline{D}$ < 3.5 nm) QDs used to assemble the dimers are necessary for ensuring an efficient overlap between the wave functions on each dot. Increasing size dispersion increases the widths in energy of the bands of excitonic states on each dot, which has a detrimental effect on the efficiency of the electronic coupling by taking the excitonic levels off resonance as shown schematically in Figures 1c and 2a and Figures S2 and S7 of the SI. A size dispersion of ≤ 5% is required to engineer electronically coupled heterodimers[15, 38-39] because of the weaker electronic coupling. In quasi-homodimers as studied here, the excitons of the two QDs are quasi-resonant, meaning that the electronic coupling is also weakened by size dispersion, albeit to a lesser extent than in heterodimers. In quasi-homodimers moderate size dispersions can actually have a positive effect, because the optical selection rules of fully dark and fully bright dimer levels of exact homodimers are broken.

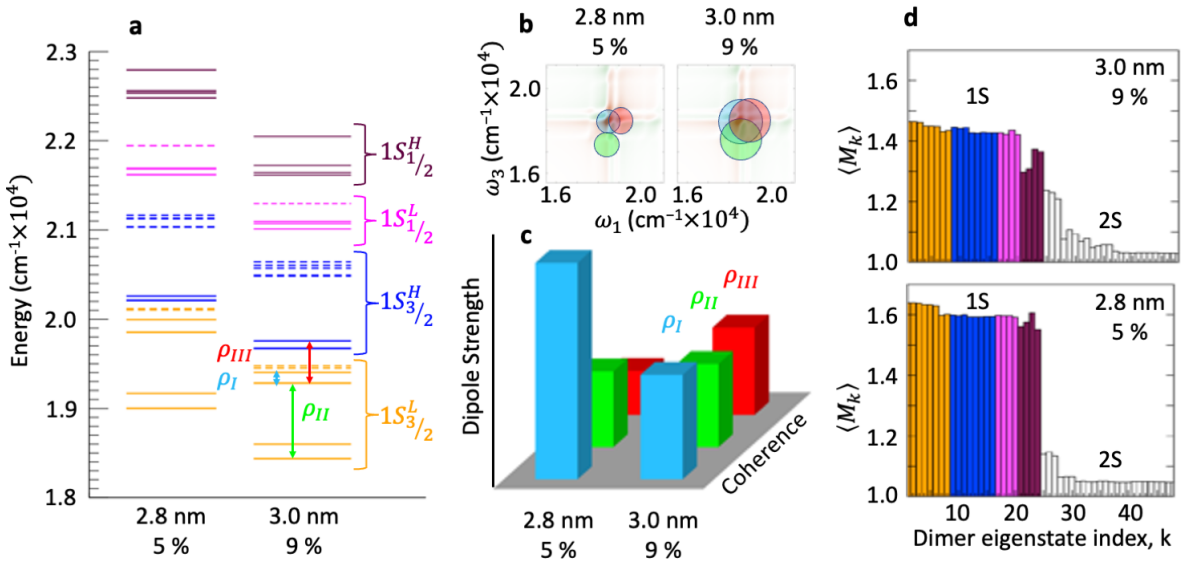

Figure 2: Comparison of the electronic properties of an ensemble of 4000 dimers of QDs with $\overline{D}$=2.8 nm and a size dispersion of 5% with those of an ensemble of dimers assembled with $\overline{D}$=3.0 nm QDs and a size dispersion of 9%. a) Energy levels of the 1S dimer exciton bands taking crystal field splitting and spin-orbit and interdot Coulomb coupling into account (see SI, section 2, and Tables S1 and S2 for the list of transition energies and associated inhomogeneous widths). Dark or low dipole strengths are drawn in dashes. The transition frequencies of the three types of electronic coherences are marked in azure, ρ_I, green, ρ_{II} and red, ρ_{III} (this color code is used throughout). b) Inhomogeneous regions in the (ω_1, ω_3) maps corresponding to the three types of coherences. c) Emission dipole strengths of the three types of electronic

coherences (see also Figure S8 of the SI). d) Interdot delocalization parameter $\langle M_k \rangle$ of the dimer states of the 1S and the 2S bands. $\langle M_k \rangle$ = 2 corresponds to the fully delocalized limit and $\langle M_k \rangle$ = 1 to the fully localized one, see Figure S3 for the SI.

Unlike in exact homodimers, in quasi-homodimers, the dipole strength is redistributed over all the dimer excitons by the electronic coupling. *This makes a larger number of electronic coherences available for quantum technology applications.* For sub-nm interparticle distances, there is therefore a range of $\overline{D}$ values and size dispersion that maximizes the number and variety of electronic coherences that can be reliably measured. For CdSe QD dimers assembled with propanedithiol ligands, our work shows that this range is between 5 to 10% size dispersion for quasi-homodimers of QDs with $\overline{D}$ ranging between 2.5 and 3 nm. We contrast the properties of quasi-homodimers for the two ends of this range in Figure 2. The mean level structures of ensembles of 4000 QD dimers with different mean diameters, $\overline{D}$ and size dispersion are computed as described in ref. [15, 37], see SI section 2. An effective mass- **k**.**p** model is used to describe the electronic states of the isolated dots and includes the spin-orbit and Coulomb coupling and crystal field splitting. The interdot Coulombic electronic interactions between the two QDs assembled with a 0.5 nm surface to surface distance lead to delocalized dimer states. Figure 2a compares the mean level structure of two kinds of the dimers: the $\overline{D}$=2.8nm/5% size disorder dimers studied previously[36-37] and the $\overline{D}$ = 3 nm/9% investigated here (results for an additional size/dispersion ensemble 2.8nm/9% are shown in Figures S3, S7 and S8). The effect of the larger size is to decrease the energies of the excited states and to a lesser extent the transition frequencies between them and that of a higher size disorder to broaden the bands.

In 2DES, frequency maps are obtained by Fourier transform (FT) of the first T_1 time interval in the pulse sequence, which leads to the abscissa ω_1. Similarly the ordinate, ω_3, is the FT along T_3[40-41] (see Figure 1d, e, f, and SI for details on the computations and additional Figures). The inhomogeneous broadening of the ground state (GS) to excited state transitions is about twice as large as in the 3nm/9% sample, which results in larger and overlapping regions of addresses corresponding to a given type of coherence in the 2DES (ω_1, ω_3) frequency maps (Figure 2b). This means that for larger amounts of size disorder, several interdot electronic coherences will beat along T_2 at the same (ω_1, ω_3) addresses on the maps, with lifetimes determined by the inhomogeneous dephasing times due to size dispersion. The larger amount of size dispersion does not quench the interdot coupling and the electronic interdot delocalization (Figure 2d). Figure 2c shows that more disorder in the ensemble leads to a more even distribution of the emission dipole strengths of the electronic coherences in the quasi-homodimer, this is because more dispersion takes us further away from the limit of the exact

dimer, with its fully bright and dark states. Increasing the size disorder while preserving sufficient interdot delocalization makes a larger set of electronic coherences observable.

3. Probing electronic coherences by multi-dimensional electronic spectroscopy

We show that the interdot electronic dynamics in the ensemble of quasi-homo dimers of CdSe QDs of controlled size dispersion can be reliably characterized experimentally in 2D and 3D-ES, both in the liquid and solid-state phase.

To uncover the complex dynamics of the electronic coherences, we also Fourier transform the dimer response along the second time interval T_2, (Figure 1f)[42-44] in the 2D (ω_1,ω_3) frequency maps. We then plot the localization of a given frequency, ω_2, in Fourier maps of the (ω_1,ω_3) plane. This Fourier analysis localizes the addresses in the (ω_1,ω_3) plane where particular frequencies beat along T_2.[41, 45-47] A given electronic coherence actually beats in a region of addresses, not merely at a single point. This is because of the inhomogeneous broadening of the GS to excited state transitions caused by the size dispersion of the QDs (Figure 2b).

Figure 3 compares computed Fourier maps to experimentally measured maps of the liquid and solid phase samples. The computed maps are obtained by first computing the polarization of the ensemble in the time domain[15] for a sequence of three phase modulated pulses[48] as a function of the three time intervals between the pulses. The polarization is then Fourier transformed along the phase modulations leading to the response in the different phase matching direction, and along the time intervals, T_1, T_2 and T_3, to obtain the Fourier maps. The Liouvillian used for the time propagation of the ensemble density matrix explicitly includes the dipolar coupling to pulses and the size dispersion of the QDs used to assemble the dimers.[15] Details about the computations of the maps are given in section S2 of the SI.

The periods of the three types of interdot electronic coherences fall in different ranges, see Tables S1 and S2 for a list of the computed transition energies and inhomogeneous widths of the electronic coherences. $\rho_I(t)$ (azure in Figure 2a) are electronic interdot coherences between fine structure (FS) dimer states of the same excitonic band, which are characterized by long periods in the 240-280 fs range (140 to 120 cm^{-1}) and long dephasing times. The ρ_I periods are longer than that of the longitudinal optical phonons (≈ 150 fs, 220 cm^{-1}) but shorter than that of the acoustic ones (20 cm^{-1})[49]. The periods of the ρ_{III} (red, Figure 2a) and ρ_{II} (green, Figure 2a) interdot coherences are governed by the interplay between the spin-orbit coupling splitting between the $1S^L_{3/2}$ and $1S^H_{3/2}$ bands, the interdot coupling strength and the spreading of the

bands due to the 9% disorder. The ρ_{III} (red) type are interdot electronic coherences between the higher energy states of the $1S_{3/2}^{L}$ band and the low ones of $1S_{3/2}^{H}$ and have periods ≈ 70 fs (480 cm^{-1}). ρ_{III} electronic coherences are intense for the 3 nm/9 % disorder dots studied here because of the more even emission dipole redistribution (Figure 2c). The ρ_{II} (green) higher transition frequencies (≈ 850 cm^{-1}), shorter period (40 fs), interdot electronic coherences take place between the low and the high energy states of the $1S_{3/2}^{L}$ band. Even faster beating electronic coherences between states in the $1S_{3/2}^{L}$ and $1S_{1/2}^{H}$ bands can be observed in the calculated results. However, their characterization in the measured data is less robust as the $1S_{1/2}^{H}$ band falls on the blue edge of the laser pulse bandwidth. See SI section 2 for computational details and additional figures.

Figures 3 a, b, and c show the computed Fourier maps for the frequency, ω_2, associated with each type of coherences, ρ_I, ρ_{III}, and ρ_{II} respectively. The maximum intensities appear at specific addresses, $(\omega_{0i}, \omega_{0j})$, that are defined by the transition frequencies of the GS to the two excited states, *i* and *j*, involved in the coherence $\rho_{ij}(t)$, as in conventional 2D frequency maps. Due to the inhomogeneous broadening of the ω_{0i} and ω_{0j} transitions, there is actually a region of addresses on the map where a specific coherence is expected to contribute. These are marked on Figures 3a, b, c with red ellipsoids, (see Table S2 for the values of the inhomogeneous broadening) and because of the 9% disorder, they overlap. For this reason, the most intense coherence, ρ_{III} (Figure 3b), appears as a background in Figure 3a and 3c. These background features cannot be resolved in the experimental maps because of extra sources of inhomogeneous broadening due to environment effects.

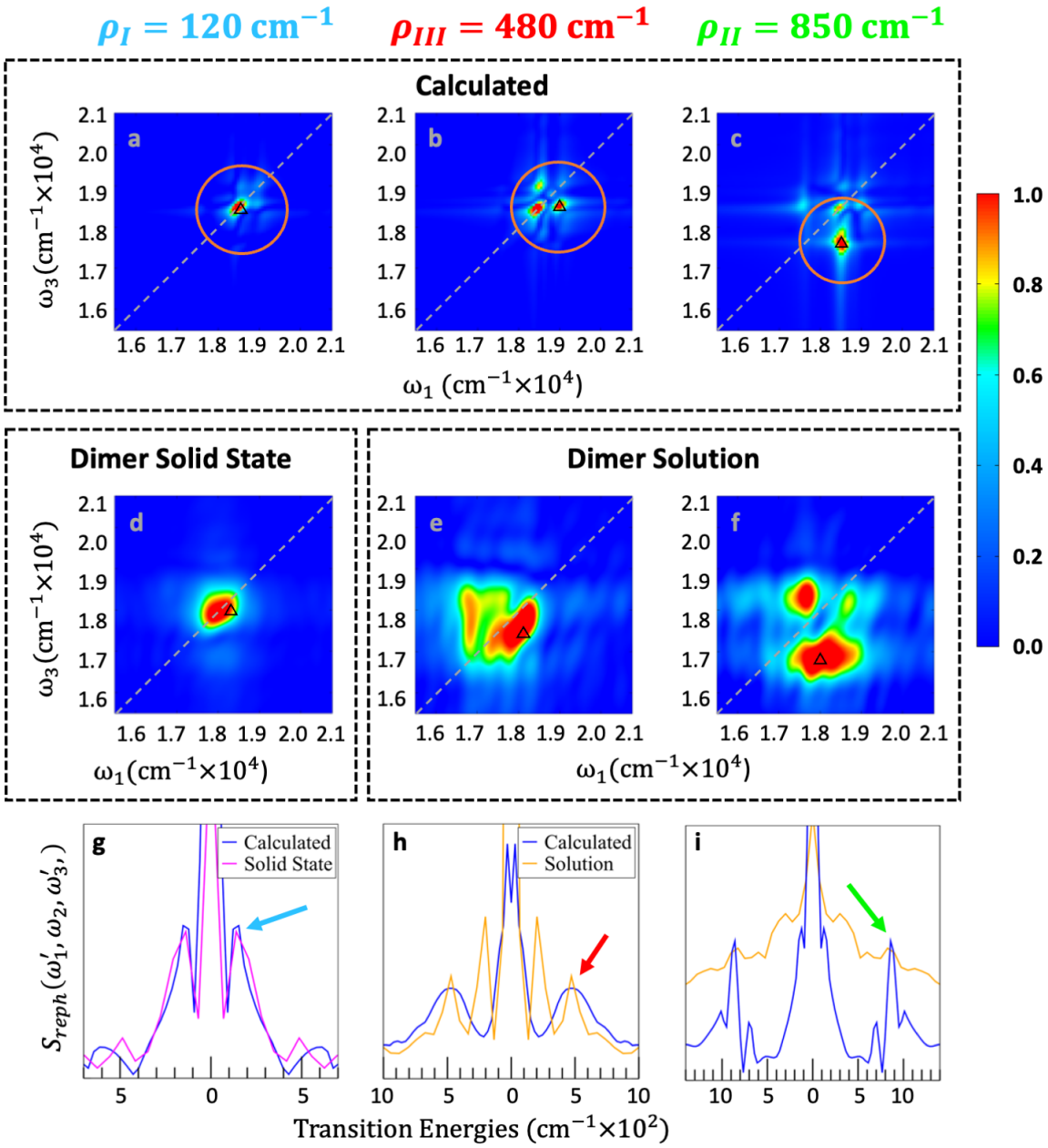

Figure 3: Top row (panels a, b, c): Computed Fourier maps in the (ω_1,ω_3) plane at three values of ω_2 corresponding to the three types of dimer electronic coherences identified in Figure 2a. Middle row (panels d, e, f): Corresponding experimental maps for the solid-state (d) and the solution (e, f) samples. Bottom row (panels g, h, i): FTs along T_2 at the addresses marked by triangles on the computed and experimental maps. The red ellipsoids on the top row indicate the extension of inhomogeneous broadening of the transitions from GS to the excited states involved in ρ_I (a), ρ_{III} (b) and ρ_{II} (c).

The Fourier map plotted in Figure 3a characterizes the type I coherence ρ_I. These are interdot coherences between delocalized FS dimer states within the lowest band, $1S^L_{3/2}$ (see Figure 2a). The position of the most intense beating of the ρ_I coherence is marked as a triangle. The excited states involved in this coherence are efficiently delocalized over the two QDs (Figure 2d). The

small transition energy of 120 cm^{-1} results in a long period of 280 fs, in a frequency range distinct from the phonon frequency of ≈ 220 cm^{-1}. There is a very good agreement between overall patterns of the coherence in the computed (Figure 3a) and solid-state maps (Figure 3d). The background pattern, seen in the computed map (Figure 3a), comes from the patterns of the ρ_{III} coherences shown in Figure 3b, which is the most intense coherence. Figure 3g shows the excellent agreement between the computed and solid-state FTs of traces at the addresses shown by the triangles in Figure 3a and d. Note that at this address, the beating of the phonon (frequency ≈ 220 cm^{-1}) appears as a small shoulder on the measured 120 cm^{-1} peak. The presence of a background due to the overlap with other coherences leads to the less intense peaks of Figure 3g, the frequencies of which correspond to the other types of coherences that also contribute at these positions. While not being the most intense, the ρ_I type interdot coherences have the longest inhomogeneous dephasing times (750 fs). This means that their beatings appear distinctly at longer times in calculated and solid-state sample traces along T_2, as shown in Figure 4a, computed at addresses close to the triangles on Figures 3a and d. The ρ_I long period coherences are effectively decoupled from the environment in the solid-state phase sample. The FT of the traces along T_2 computed for the solution sample is compared with the solid-state and calculated ones in Figure S13. In the solution sample, the optical phonon frequency is dominant and the ρ_I frequency is less intense. The ρ_I low frequency also appears as a shoulder in the FT of the trace of the solution sample taken at the address of the ρ_{II} coherence (Figure 3i), see below.

The Fourier maps of the ρ_{III} electronic coherences are shown in Figures 3b and 3e. These coherences have shorter periods than the ρ_I type, in the range of 70 fs (transition energies ≈480 cm^{-1}). ρ_{III} coherences are clearly identified in the liquid phase (Figure 3e) and solid-state samples. The region of the most intense ρ_{III} coherence beating is marked in Figures 3b and 3f with triangles. The FTs of the computed and experimental solution traces along T_2 at the address of the triangles are compared in Figure 3i, with excellent agreement. There is also an excellent agreement with the FT of the solid-state sample shown in Figure S14. The peak at low frequency (≈ 220 cm^{-1}) on the experimental FT plot for the solution corresponds to the optical phonon mode, which is not included in the computations.

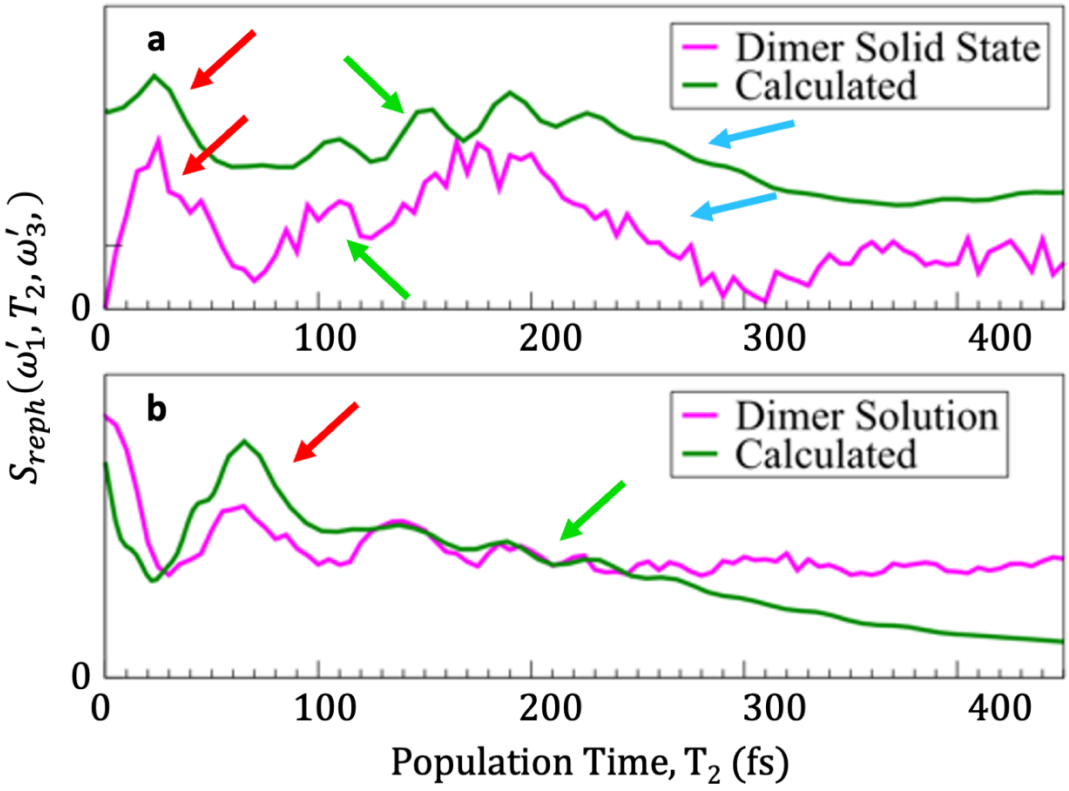

Figure 4: Comparison between the computed and measured traces extracted at coordinates close to triangles in figures 3b and e a) (18566 cm^{-1}, 18324 cm^{-1}) and (18203 cm^{-1}, 17573 cm^{-1}), b) (19163 cm^{-1}, 18808 cm^{-1}) and (17905 cm^{-1}, 17018 cm^{-1}). One clearly sees the effect of the dephasing times of the three types of coherence (marked with azure, red and green arrows) whose characteristic regions of addresses overlap because of size dispersion.

Figures 3c, f and i characterize the ρ_{II} interdot coherences. These coherences have shorter periods of ≈ 40 fs (850 cm^{-1}) with inhomogeneous dephasing times of approximately 275 fs. This dephasing time is between those of the ρ_I coherences, ≈ 750 fs, and the ρ_{III} coherences, ≈ 115 fs. Figures 3c and 3f show the computed and experimental solution maps, respectively. The most intense beating of ρ_{II} occurs at the same position on both maps, marked with triangles. There is an excellent agreement between the patterns of the computed and measured maps which is confirmed by the FT transforms of the traces along T_2 at these points, compared in Figure 3i. At this address, the ρ_{II} coherence dominates the signal in the FT. In Figure 3i, satellite peaks are also distinguishable at slightly lower and higher frequencies. These correspond to other coherences between states of the $1S_{3/2}^{L}$ band. The FT of the solid-state sample is also in excellent agreement as shown in Figure S15. Note that on Figure 3i, the low frequency of the ρ_I coherence appears as a shoulder in the FT of both the computed and the experimental solution signals. In the solution signal, one also sees the optical phonon

frequency. The low ρ_I frequency also appears very clearly in the FT of the solid sample shown in Figure S15. This is a consequence of the overlap of the regions specific of each type of coherences due to inhomogeneous broadening.

The fact that several coherences can beat at the same address in the (ω_1,ω_3) plane is emphasized in Figure 4, which compares T_2 traces of the computed and measured samples at specific frequency addresses. The beating periods of all three coherence types can be clearly distinguished in the traces on Figure 4a taken at addresses in the vicinity of the triangles in Figures 3a and 3d. Figure 4a unambiguously confirms that the ρ_I, ρ_{II} and ρ_{III} coherences beat in the measured solid-state trace with distinctive periods of 280 fs, 40 fs and 70 fs respectively. Figure 4b compares traces in the (ω_1,ω_3) plane in the vicinity of the triangles in Figures 2b and 2e for the solution sample. The 70 fs period of the ρ_{III} coherence appears very clearly in the calculated and measured solution traces at short times, but is replaced at longer times by the 40 fs period of the ρ_{II}. This behavior is due to the relative values of the dephasing times of ρ_{II} and ρ_{III}. In general, the comparison between the calculated and measured traces in solution and in the solid-state is excellent, which confirms that the individuality of the dimers is well preserved in the multilayered thin films.

4 Conclusions

We have shown that it is possible to reliably characterize interdot electronic coherences measured by 2DES in ensembles of CdSe QD quasi-homodimers, assembled from small 3nm QDs with 9% size disorder, in the liquid and solid phase. Provided that effective interdot electronic delocalization is ensured by using small (< 3.5 nm) sizes and that the dimers are assembled at sub-nm distance, higher amounts of disorder have the beneficial effect of breaking the optical selection rules and leading to a wider range and larger number of observable electronic coherences. In the 3nm/9% ensemble of quasi-homodimers, more than one type of interdot electronic coherence will beat at specific addresses on the 2D frequency maps leading to richer and more complex electronic coherence dynamics. These disorder controlled features open up new prospects for exploitation in quantum technologies.

Acknowledgements

We thank Dr. Hugo Gattuso for discussions on the modeling. This work was financially supported by the H2020 FET Project COPAC (#766563). EC acknowledges partial support by

‘CQ-TECH’ STARS Grant 2019 (2019-UNPD0Z9- 0166571). FR and JH acknowledge the support of the Consortium des Equipements de Calcul Intensif (CECI), funded by the F.R.S.-FNRS (Fonds National de la recherche Scientifique, Belgium) under Grant #2.5020.11 for the computations and support of F.R.S-FNRS through the grant PDR # T.0205.20.

Supplementary information is available free of charge. It provides details about the computational and experimental methods for 2DES, the fabrication of the samples and supplementary figures.

Conflict of interest: The authors declare no conflict of interest

Data availability: The experimental and computational data are available upon request

References

[1]L. Brus, *J. Phys. Chem.* **1986**, *90*, 2555-2560.
[2]V. I. Klimov, CRC Press, Boca Raton, **2010**.
[3]A. P. Alivisatos, *Science* **1996**, *271*, 933.
[4]C. R. Kagan, C. B. Murray, M. Nirmal, M. G. Bawendi, *Phys. Rev. Lett.* **1996**, *76*, 1517-1520.
[5]C. B. Murray, C. R. Kagan, M. G. Bawendi, *Ann. Rev. Mater. Sci.* **2000**, *30*, 545-610.
[6]D. J. Norris, M. G. Bawendi, *Phys. Rev. B* **1996**, *53*, 16338-16346.
[7]M. V. Kovalenko, L. Manna, A. Cabot, Z. Hens, D. V. Talapin, C. R. Kagan, V. I. Klimov, A. L. Rogach, P. Reiss, D. J. Milliron, P. Guyot-Sionnnest, G. Konstantatos, W. J. Parak, T. Hyeon, B. A. Korgel, C. B. Murray, W. Heiss, *ACS Nano* **2015**, *9*, 1012-1057.
[8]O. V. Prezhdo, *Acc. Chem. Res.* **2009**, *42*, 2005-2016.
[9]C. R. Kagan, L. C. Bassett, C. B. Murray, S. M. Thompson, *Chem. Rev.* **2021**, *121*, 3186-3233.
[10]E. Collini, *J. Phys. Chem. C* **2021**, *125*, 13096-13108.
[11]S. Koley, J. Cui, Y. E. Panfil, U. Banin, *Acc. Chem. Res.* **2021**, *54*, 1178-1188.
[12]D. Spittel, J. Poppe, C. Meerbach, C. Ziegler, S. G. Hickey, A. Eychmüller, *ACS Nano* **2017**, *11*, 12174-12184.
[13]P. Rebentrost, M. Stopa, A. Aspuru-Guzik, *Nano Lett.* **2010**, *10*, 2849-2856.
[14]K. Komarova, H. Gattuso, R. D. Levine, F. Remacle, *J. Phys. Chem. Lett.* **2020**, *11*, 6990-6995.
[15]H. Gattuso, R. D. Levine, F. Remacle, *Proc. Natl. Acad. Sci. USA* **2020**, *117*, 21022.
[16]K. Komarova, H. Gattuso, R. D. Levine, F. Remacle, *Front. Phys.* **2020**, *8*, 486.
[17]F. P. García de Arquer, V. Talapin Dmitri, I. Klimov Victor, Y. Arakawa, M. Bayer, H. Sargent Edward, *Science*, *373*, eaaz8541.
[18]J. R. Caram, H. Zheng, P. D. Dahlberg, B. S. Rolczynski, G. B. Griffin, A. F. Fidler, D. S. Dolzhnikov, D. V. Talapin, G. S. Engel, *J. Phys. Chem. Lett.* **2014**, *5*, 196-204.
[19]D. B. Turner, Y. Hassan, G. D. Scholes, *Nano Lett.* **2012**, *12*, 880-886.
[20]E. Cassette, J. C. Dean, G. D. Scholes, *Small* **2016**, *12*, 2234-2244.
[21]N. Lenngren, M. A. Abdellah, K. Zheng, M. J. Al-Marri, D. Zigmantas, K. Žídek, T. Pullerits, *Phys. Chem. Chem. Phys.* **2016**, *18*, 26199-26204.
[22]E. Collini, H. Gattuso, L. Bolzonello, A. Casotto, A. Volpato, C. N. Dibenedetto, E. Fanizza, M. Striccoli, F. Remacle, *J. Phys. Chem. C* **2019**, *123*, 31286-31293.

[23]S. Palato, H. Seiler, P. Nijjar, O. Prezhdo, P. Kambhampati, *Proc. Natl. Acad. Sci. USA* **2020**, *117*, 11940-11946.
[24]Z. Wang, N. Lenngren, E. Amarotti, A. Hedse, K. Žídek, K. Zheng, D. Zigmantas, T. Pullerits, *J. Phys. Chem. Lett.* **2022**, *13*, 1266-1271.
[25]S. Dong, D. Trivedi, S. Chakrabortty, T. Kobayashi, Y. Chan, O. V. Prezhdo, Z.-H. Loh, *Nano Lett.* **2015**, *15*, 6875-6882.
[26]E. Cohen, I. Gdor, E. Romero, S. Yochelis, R. van Grondelle, Y. Paltiel, *J. Phys. Chem. Lett.* **2017**, *8*, 1014-1018.
[27]C. R. Kagan, C. B. Murray, *Nat. Nanotechnol.* **2015**, *10*, 1013-1026.
[28]C. B. Murray, C. R. Kagan, M. G. Bawendi, *Science* **1995**, *270*, 1335.
[29]T. Lee, K. Enomoto, K. Ohshiro, D. Inoue, T. Kikitsu, K. Hyeon-Deuk, Y.-J. Pu, D. Kim, *Nat. Commun* **2020**, *11*, 5471.
[30]H. Döllefeld, H. Weller, A. Eychmüller, *Nano Lett.* **2001**, *1*, 267-269.
[31]J. Cui, Y. E. Panfil, S. Koley, D. Shamalia, N. Waiskopf, S. Remennik, I. Popov, M. Oded, U. Banin, *Nat. Commun* **2019**, *10*, 5401.
[32]C. N. Dibenedetto, E. Fanizza, R. Brescia, Y. Kolodny, S. Remennik, A. Panniello, N. Depalo, S. Yochelis, R. Comparelli, A. Agostiano, M. L. Curri, Y. Paltiel, M. Striccoli, *Nano Res.* **2020**, *13*, 1071-1080.
[33]C. N. Dibenedetto, E. Fanizza, L. De Caro, R. Brescia, A. Panniello, R. Tommasi, C. Ingrosso, C. Giannini, A. Agostiano, M. L. Curri, M. Striccoli, *Mater. Res. Bull.* **2022**, *146*, 111578.
[34]J. C. Dean, G. D. Scholes, *Acc. Chem. Res.* **2017**, *50*, 2746-2755.
[35]K. M. Pelzer, G. B. Griffin, S. K. Gray, G. S. Engel, *J. Chem. Phys.* **2012**, *136*, 164508.
[36]E. Collini, H. Gattuso, Y. Kolodny, L. Bolzonello, A. Volpato, H. T. Fridman, S. Yochelis, M. Mor, J. Dehnel, E. Lifshitz, Y. Paltiel, R. D. Levine, F. Remacle, *J. Phys. Chem. C* **2020**, *124*, 1622-16231.
[37]E. Collini, H. Gattuso, R. D. Levine, F. Remacle, *J. Chem. Phys.* **2021**, *154*, 014301.
[38]H. Gattuso, B. Fresch, R. D. Levine, F. Remacle, *Appl. Sci.* **2020**, *10*, 1328.
[39]E. Cohen, P. Komm, N. Rosenthal-Strauss, J. Dehnel, E. Lifshitz, S. Yochelis, R. D. Levine, F. Remacle, B. Fresch, G. Marcus, Y. Paltiel, *J. Phys. Chem. C* **2018**, *122*, 5753-5758.
[40]A. M. Brańczyk, D. B. Turner, G. D. Scholes, *Annalen der Physik* **2014**, *526*, 31-49.
[41]T. R. Calhoun, N. S. Ginsberg, G. S. Schlau-Cohen, Y.-C. Cheng, M. Ballottari, R. Bassi, G. R. Fleming, *J. Phys. Chem. B* **2009**, *113*, 16291-16295.
[42]D. B. Turner, K. W. Stone, K. Gundogdu, K. A. Nelson, *J. Chem. Phys.* **2009**, *131*, 144510.
[43]H. Li, A. D. Bristow, M. E. Siemens, G. Moody, S. T. Cundiff, *Nat. Commun* **2013**, *4*, 1390-1390.
[44]S. Irgen-Gioro, A. P. Spencer, W. O. Hutson, E. Harel, *J. Phys. Chem. Lett.* **2018**, *9*, 6077-6081.
[45]D. B. Turner, R. Dinshaw, K.-K. Lee, M. S. Belsley, K. E. Wilk, P. M. G. Curmi, G. D. Scholes, *Phys. Chem. Chem. Phys.* **2012**, *14*, 4857-4874.
[46]F. Milota, V. I. Prokhorenko, T. Mancal, H. von Berlepsch, O. Bixner, H. F. Kauffmann, J. Hauer, *J. Phys. Chem. A* **2013**, *117*, 6007-6014.
[47]N. Christensson, K. Žídek, N. C. M. Magdaong, A. M. LaFountain, H. A. Frank, D. Zigmantas, *J. Phys. Chem. B* **2013**, *117*, 11209-11219.
[48]P. Kjellberg, B. Brüggemann, T. Pullerits, *Phys. Rev. B* **2006**, *74*, 024303.
[49]A. J. Mork, E. M. Y. Lee, W. A. Tisdale, *Phys. Chem. Chem. Phys.* **2016**, *18*, 28797-28801.